Gap Filling of Missing Data for VIIRS Global Ocean Color Products Using the DINEOF Method

Xiaoming Liu and Menghua Wang

Abstract—**Ocean color data are critical for the monitoring and understanding of biological and ecological processes and phenomena, and the data are also important sources of input data for physical and biogeochemical ocean models. The Visible Infrared Imaging Radiometer Suite (VIIRS) onboard the Suomi National Polar-orbiting Partnership (SNPP) has continued to provide global ocean color data since its launch in October 2011. However, there are always many missing pixels in the original VIIRS-measured ocean color images due to clouds and various other reasons. The Data Interpolating Empirical Orthogonal Functions (DINEOF) is a method to reconstruct (gap-filling) missing data in geophysical datasets based on the Empirical Orthogonal Function (EOF). In this study, the DINEOF is applied to VIIRS-derived global Level-3 binned ocean color data of 9-km spatial resolution, and the DINEOF reconstructed ocean color data are used to fill the gaps of missing data. In particular, daily, 8-day, and monthly VIIRS global Level-3 binned ocean color data, including chlorophyll-a (Chl-a) concentration, diffuse attenuation coefficient at 490 nm (K_d(490)), as well as normalized water-leaving radiance spectra ($nL_w(\lambda)$) at the five VIIRS visible bands, are tested and evaluated. To validate and evaluate the gap-filled data, a set of original valid non-missing pixels in the VIIRS images are selected randomly and treated as missing pixels in the DINEOF process, so that the reconstructed pixels can be compared with the original data. Results show that the DINEOF method can successfully reconstruct and gap-fill meso-scale and large-scale spatial ocean features in the global VIIRS Level-3 images, as well as capture the temporal variations of these features.**

Index Terms—**Ocean color remote sensing, VIIRS, gap-filling missing data, DINEOF**

I. INTRODUCTION

OCEAN color data from satellite sensors such as the Sea-viewing Wide Field-of-view Sensor (SeaWiFS) [1], the Moderate Resolution Imaging Spectroradiometer (MODIS) on the Terra and Aqua satellites [2, 3], the Medium Resolution Imaging Spectrometer (MERIS) on the Envisat [4], the Visible Infrared Imaging Radiometer Suite (VIIRS) onboard the Suomi National Polar-orbiting Partnership (SNPP) [5, 6] and NOAA-20, and the Ocean and Land Colour Instrument (OLCI) on the Sentinel-3A satellite are critical for the monitoring and understanding of ocean biological and ecological processes and phenomena, and they are also required input data for physical and biogeochemical ocean models. For example, the satellite-derived water diffuse attenuation coefficient for the

photosynthetically available radiation (PAR), K_d(PAR), is used to estimate heat flux within the upper water column in global and regional ocean numerical models [7]. Since the SNPP launch in October 2011, VIIRS ocean color products have been routinely produced globally [6, 8]. The standard VIIRS ocean color product suite includes normalized water-leaving radiance spectra $nL_w(\lambda)$ [9, 10], chlorophyll-a (Chl-a) concentration [11-13], water diffuse attenuation coefficient at the wavelength of 490 nm K_d(490) and at PAR K_d(PAR) [14, 15], as well as many experimental products such as inherent optical properties (IOPs) [16] and a newly added QA score product for measuring data quality [17]. In addition, VIIRS global ocean color products using the shortwave infrared (SWIR)-based and near-infrared (NIR)-SWIR combined ocean color data processing approaches have been routinely produced [18, 19], which improve ocean color data quality over turbid coastal and inland waters [20-22]. Furthermore, VIIRS ocean color data processing algorithms have been significantly improved, including enhanced sensor on-orbit calibration using both solar and lunar approaches [23]. In July 2017, NOAA declared operational status for VIIRS ocean color products.

However, for global ocean color products similar to those from SeaWiFS, MODIS, MERIS, OLCI, and other ocean color satellite sensors, there are always missing pixels in the VIIRS-measured ocean color data imageries due to cloud cover [24, 25] and various other reasons, e.g., strong sun glint contamination [26], dust storms, very large solar- and sensor-zenith angles, etc. It is certainly useful to gap-fill the missing pixels before the data are used as input for ocean models and for some other applications. In fact, it is usually a requirement to complete a filled (no-gap) data set for model input. For example, the Empirical Orthogonal Function (EOF) analysis is a method to determine a set of orthogonal functions that characterizes the co-variability of a time series for a set of grid points [27]. It is often used to study possible spatial modes (patterns) of variability and to learn how they change with time. Traditional EOF analysis operates on matrices and requires a complete array of data without gaps in the matrices.

To reconstruct missing pixels in the remote sensing data, various methods have been developed in several previous studies. *Shen et al.* [28] reviewed and summarized these established and emerging reconstruction methods, and suggested that they can be classified into four categories: (1) spatial-based methods, (2) spectral-based methods, (3)

Submitted on 9/25/2017

Xiaoming Liu (e-mail: Xiaoming.Liu@noaa.gov) and Menghua Wang (e-mail: Menghua.Wang@noaa.gov) are both with the Center for Satellite Applications and Research, NESDIS/NOAA, 5830 University Research Court, College Park, MD 20746, USA. Xiaoming Liu is also affiliated with CIRA at Colorado State University, Fort Collins, CO 80523, USA.

temporal-based methods, and (4) hybrid methods [28]. In their study, these algorithms were also applied to a few other useful applications for reconstruction of missing pixels in remote sensing data, and the strengths and weaknesses of each method were surveyed theoretically and experimentally.

The Data Interpolating Empirical Orthogonal Functions (DINEOF) [29, 30] is an EOF-based technique developed to reconstruct missing data in geophysical datasets. It exploits the spatio-temporal coherency of the data to infer a value at the missing location, and has been successfully applied in various applications [30-36]. In fact, the DINEOF method has been applied to ocean color data from MODIS [37-39], the Spinning Enhanced Visible and Infrared Imager (SEVIRI) onboard the Meteosat Second Generation 2 [40], and the Korean Geostationary Ocean Color Imager (GOCI) [41]. The DINEOF-derived results have also been compared with other gap-filling methods to assess their accuracy. *Henn et al.* [42] compared the DINEOF method with a method based on temporal interpolation and with three other methods based on spatial Kriging and Least-Squares-Fit. It was concluded that DINEOF was the most accurate method for applications with a large number of stations and grids [42], which is also applicable to the case of satellite remote sensing data.

As VIIRS ocean color products become operational and used more frequently by operational users in the future, filling the gap of missing pixels in the VIIRS ocean color data imageries will be increasingly necessary and useful. In addition, the previous DINEOF applications were mostly focused on regional oceans, and no former studies were found that use the DINEOF to reconstruct global ocean color data. In this study, the DINEOF method is used to reconstruct and gap-fill global VIIRS daily, 8-day, and monthly ocean color product data, including Chl-a, $K_d(490)$, and $nL_w(\lambda)$ at the VIIRS-SNPP five visible bands (i.e., 410, 443, 486, 551, and 671 nm). With the reconstructed (gap-filled) VIIRS global daily Chl-a images, ocean features can now be well identified and observed both spatially and temporally. Some examples that demonstrate advantages and usefulness of the gap-filled VIIRS global ocean color products are provided. Furthermore, the DINEOF reconstructed non-gap VIIRS global daily, 8-day, and monthly ocean color images with some validation and evaluation results are presented and discussed.

II. DATA AND METHODS

A. VIIRS Global Level-3 Ocean Color Data

The Multi-Sensor Level-1 to Level-2 (MSL12), which is the official NOAA VIIRS ocean color data processing system, has been used for processing VIIRS data from Sensor Data Records (SDR or Level-1B data) to the Environmental Data Records (EDR or Level-2 data) [6, 8]. MSL12 was originally developed for the purpose of using a consistent and common ocean color data processing system to process global ocean color data from multiple satellite ocean color sensors [43-45]. Specifically, MSL12 is based on the SeaWiFS Data Analysis System (SeaDAS) version 4.6 with some significant improvements, including the SWIR- and NIR-SWIR-based atmospheric

correction algorithms for improved satellite ocean color data over coastal and inland waters [18-20]. There are also many studies and applications using the SWIR-based ocean color data processing over global highly turbid coastal and inland waters [21, 46-51]. In fact, MSL12 has been routinely producing VIIRS-NOAA-20 global ocean color products since its door opened on December 13, 2017. In addition, since July 2012, MSL12 has been used for the routine production of NOAA operational ocean color products from MODIS-Aqua over the 12 NOAA CoastWatch regions (i.e., various U.S. open oceans, and coastal, and inland waters) [52] (www.ospo.noaa.gov/Products/ocean/). Furthermore, MSL12 has been used to process ocean color products from the GOCI [53]. Certainly, MSL12 will also be used for producing ocean color products from all future VIIRS sensors onboard the Joint Polar Satellite System (JPSS) series, e.g., JPSS-2, JPSS-3, etc.

The VIIRS global Level-3 ocean color product data are generated using the spatial and temporal binning from the corresponding Level-2 data. The Level-3 data processing algorithm is essentially the same as the one used for producing SeaWiFS and MODIS global Level-3 ocean color products [54]. Specifically, in the Level-3 data processing, pixels containing valid Level-2 data are mapped to a fixed spatial grid with spatial resolution of 9×9 km^2. The grid elements or bins are arranged in rows beginning at the South Pole. Each row begins at 180° longitude and circumscribes Earth at a given latitude. Within each bin, the statistics of mean or median are accumulated for periods of one day, eight days, and one month (or for any time periods). Before the binning process, several Level-2 data quality flags from MSL12 (mainly high solar-zenith angle, high sensor-zenith angle, high sun glint [26], stray-light/cloud shadowing [55], and ice contamination [56]) are applied to VIIRS ocean color Level-2 data. In this study, VIIRS global Level-3 binned data of 9-km spatial resolution in January, April, July, and October of 2014 are used. These four months represent four seasons in VIIRS-derived global ocean color data. Figure 1 shows examples of the global Level-3 daily Chl-a images for January 15 (Fig. 1a), April 15 (Fig. 1b), July 15 (Fig. 1c), and October 15 (Fig. 1d) of 2014. Obviously, there are many missing pixels in the VIIRS Chl-a images. In fact, there are ~70% pixels missing in these global daily images due to cloud cover, high sun glint contamination, high solar- or sensor-zenith angles, and various other reasons.

B. Applications of the DINEOF Method on VIIRS Global Level-3 Data

The DINEOF method [29, 30] is an EOF-based technique, which identifies and utilizes dominant spatial and temporal patterns in geophysical datasets to reconstruct missing data. The DINEOF procedure can be summarized as the following:

(a) First, initial data are obtained through subtracting the mean value from the entire data set and setting the missing data to zero.

(b) Next, the EOF is performed to the data set, and the missing data are replaced with the initial guess by the data reconstruction using the spatial and temporal functions of only
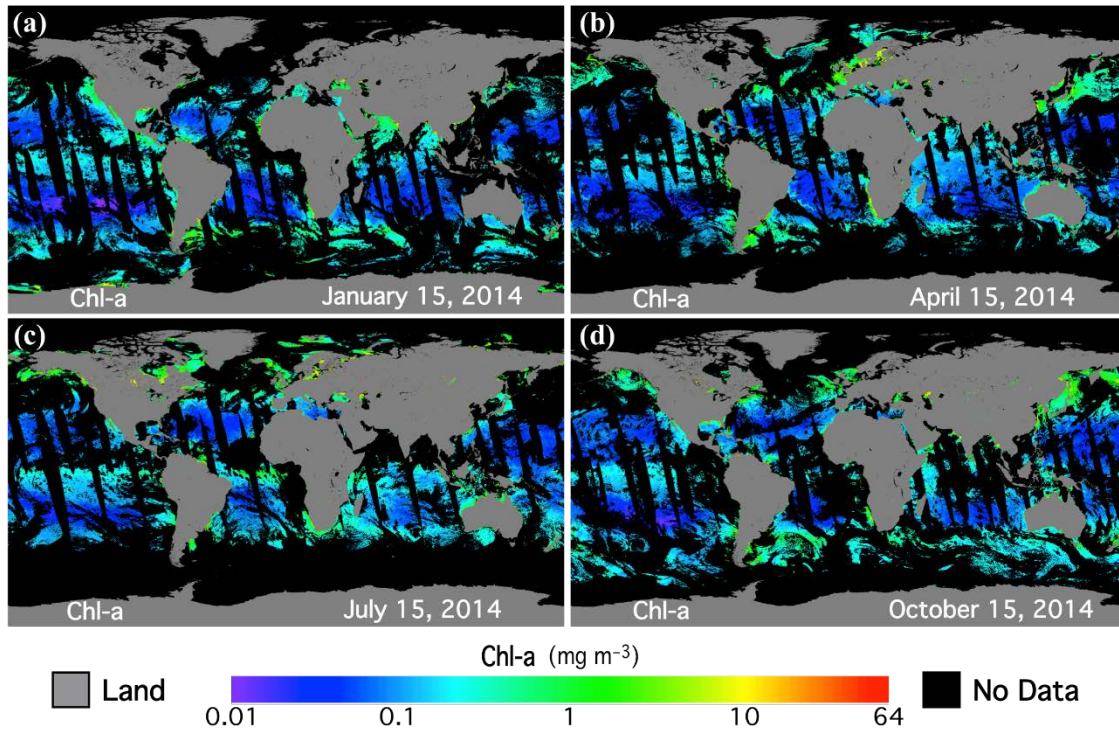
Fig. 1. Original VIIRS-derived global daily Chl-a images for the dates of (a) January 15, (b) April 15, (c) July 15, and (d) October 15, 2014. These VIIRS Chl-a data and images were generated from the MSL12 and VIIRS global daily Level-3 binned data.
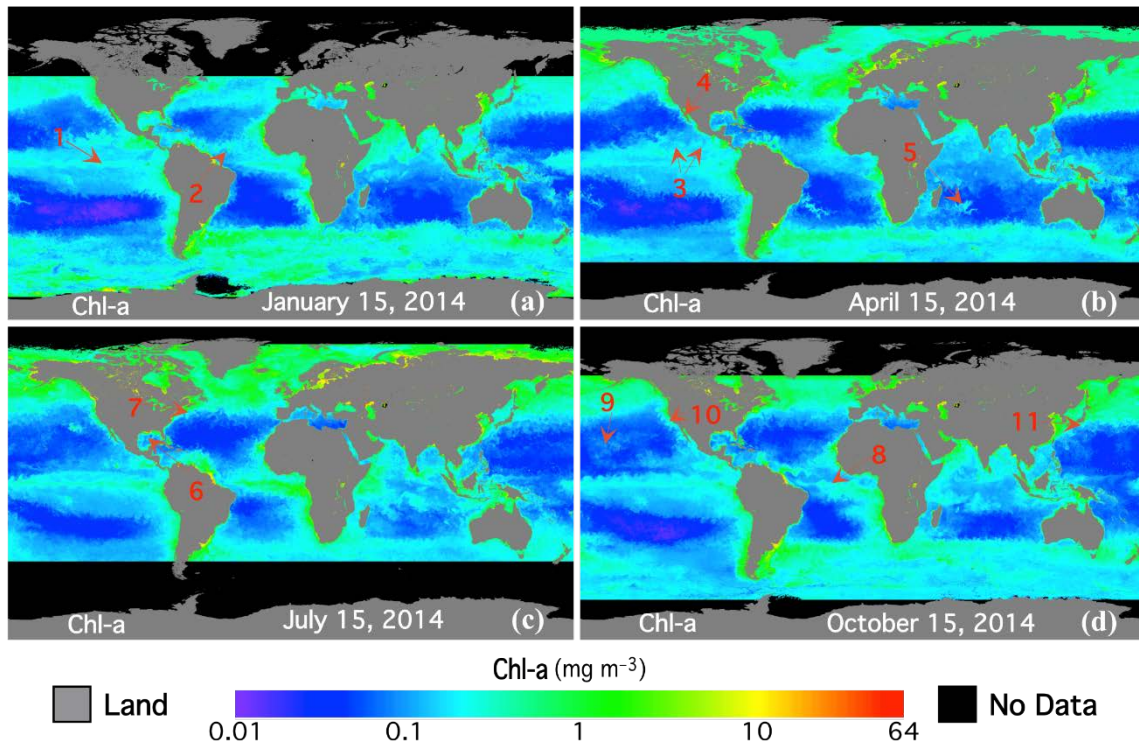

Fig. 2. Fully reconstructed (gap-filled) VIIRS global daily Chl-a images using the DINEOF method for the dates of (a) January 15, (b) April 15, (c) July 15, and (d) October 15, 2014. Examples of the 11 meso-scale ocean features revealed in the reconstructed global VIIRS daily Chl-a images are indicated.

the first EOF mode.

(c) Finally, the first EOF mode is recalculated iteratively using the previous best guess as the initial value of the missing data for the subsequent iteration until the process converges.

This procedure is repeated iteratively with n EOF modes (n = 1, 2, 3, …) until it reaches convergence. At each step, a cross-validation method is used to calculate the final optimum number of EOF modes to retain, so that the cross-validation

error is minimum. It should be noted that not all EOF modes are used in the final data reconstruction, and the noise, as well as small scale and transient features in the high order EOF modes, are removed from the reconstructed data. *Henn et al.* [39] provided a very useful and more detailed pseudo code algorithm of the DINEOF method in their appendix. The complete and detailed description about the DINEOF technique can be found in *Beckers and Rixen* [29] and *Alvera-Azcarate et al.* [30].

The original DINEOF package was used to reconstruct (gap-fill) the missing pixels in the VIIRS global Level-3 daily, 8-day, and monthly ocean color data. It is noted that DINEOF is applied directly to the VIIRS Level-3 bin data files, instead of the mapped data files. As described in the previous section, the number of bins is different for each row of the VIIRS Level-3 data, so they are not in the standard matrix. Therefore, a preprocessor is developed to reorganize the Level-3 bins before being used as input of DINEOF. In the preprocessing, bins in all Level-3 data files are put into an $m \times n$ matrix, where m is the number of bins in the region (spatial), and n is the number of Level-3 data files in the time series (temporal). In the meantime, land mask is applied to extract ocean pixels. DINEOF is then applied on the $m \times n$ matrix to fill the gap pixels. Similarly, a postprocessor is also developed to convert the $m \times n$ matrix back into Level-3 bin format after the DINEOF process.

First, DINEOF is applied to one month of daily data in the month of January, April, July, October of 2014, separately. However, due to the limitation (cut off) for high solar-zenith angle, there are no pixels available for the entire month in the large areas of northern high latitude region in January and southern high latitude region in July. Thus, the missing pixels in these high latitude areas cannot be reconstructed. Since there are about 6 million bins in each daily global Level-3 data file with 9-km spatial resolution, performing the DINEOF on the entire global dataset is very inefficient. Therefore, in the preprocessing, the global dataset is evenly divided into 16 zonal sections between 80°S and 80°N at every 10°, i.e., 80°S–70°S, 70°S–60°S, …, 60°N–70°N, and 70°N–80°N, and DINEOF is applied to each of zonal sections separately. In fact, DINEOF is applied to these 16 zonal sections simultaneously to improve data processing efficiency. Since a 10-degree zonal section is large enough to capture both large and meso-scale spatial features, the major EOF modes in each zonal section are kept, and the impact on the final results can be neglected. In the postprocessing, the 16 zonal sections are recombined into one global Level-3 file. After global Level-3 gap-filled daily data are generated, global Level-3 8-day and monthly data can then be generated from these gap-filled daily data. It is noted that this procedure is repeated for each of the seven VIIRS ocean color products, i.e., Chl-a, $K_d(490)$, $nL_w(410)$, $nL_w(443)$, $nL_w(486)$, $nL_w(551)$, and $nL_w(671)$.

III. RESULTS

A. Gap Filling for VIIRS Global Daily Chl-a Data

We define the terminology for three types of images: original image, reconstructed image, and filled image. Original image is

TABLE I. MEAN, MEDIAN AND STD OF RECONSTRUCTED/ORIGINAL RATIO OF CHL-A FOR JANUARY 15, APRIL 15, JULY 15, AND OCTOBER 15 OF 2014.

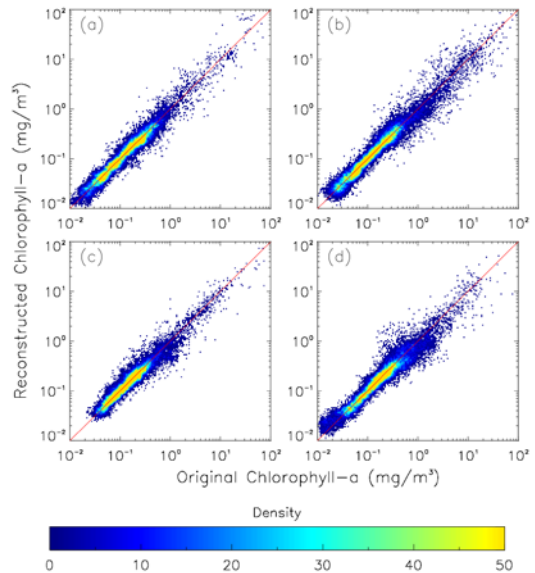| Date in 2014	Mean	Median	STD
January 15	1.022	0.996	0.261
April 15	1.033	0.996	0.319
July 15	1.015	0.986	0.246
October 15	1.021	0.985	0.354

Fig. 3. Density-scatter plots of global reconstructed versus original Chl-a data for the dates of (a) January 15, (b) April 15, (c) July 15, and (d) October 15, 2014.

from the original VIIRS global Level-3 binned data, which contain missing data. Reconstructed image is calculated from the retained EOF modes using the DINEOF method [29]. In the reconstructed image, all ocean color data are reconstructed on every ocean pixel (including valid non-missing pixels). The reconstructed image has no-gap spatially. However, there are some small differences between reconstructed and original data even for non-missing pixels due to truncated EOF modes in computing all data values. The filled image is a combination of the original image and the reconstructed image, i.e., missing pixels are filled with reconstructed data and original data are kept for non-missing pixels. As examples, Figure 2 shows the fully reconstructed global daily Chl-a images of the same dates as in Fig. 1, i.e., January 15 (Fig. 2a), April 15 (Fig. 2b), July 15 (Fig. 2c), and October 15 (Fig. 2d) of 2014. All gaps in the original images (see Fig. 1) are now reconstructed (filled), and the transitions between the gap and non-gap pixels are smooth spatially. Due to high solar-zenith angles (> 70°), there are no observations for January (July) in the northern (southern) high latitude region in the entire month, and therefore, the missing data in these regions could not be filled using the DINEOF process.

To quantitatively evaluate the accuracy of the DINEOF data reconstruction method, a set of valid pixels are intentionally

TABLE II. LIST OF SOME MESO-SCALE OCEAN FEATURES REVEALED IN THE RECONSTRUCTED VIIRS GLOBAL CHL-A IMAGES.

Number	Description	Location	Figure
1	Tropical instability waves (equatorial Pacific)	Equator	2a
2	North Brazil Current ring	9.18°N & 54.23°W	2a
3	Spin-off eddies in the tropical Pacific Ocean	10°N & 100°W	2b
4	Eddies associated with costal current near Baja	27°N & 115°W	2b
5	Madagascar plumes	26°S & 58°E	2b
6	Loop Current and associated eddies	26°N & 88°W	2c
7	Gulf Stream and associated eddies	39°N & 68°W	2c
8	Tropical instability waves (equatorial Atlantic)	6°N & 42°W	2d
9	Eddies generated near Hawaii	21°S & 163°W	2d
10	Eddies of California Coastal Current	38°N & 128.5°W	2d
11	Eddies of Kuroshio	32°N & 141°E	2d

treated as "missing pixels," so that DINEOF-reconstructed data can be compared with the original data. Specifically, before the DINEOF process, 5% of the valid (non-missing) pixels are purposely removed from the original global Level-3 data on January 15, April 15, July 15, and October 15 of 2014. The locations of these validation pixels are randomly selected using the random number generator in the Interactive Data Language (IDL). It is noted that 5% taken from the valid pixels in the original images in Fig. 1 is quite a significant amount since only ~30% of the pixels are valid pixels in global oceans. After the DINEOF process, these data are reconstructed and compared with the original data. Figure 3 shows the density scatter plots of the reconstructed data versus original data, which show that most points are close to the 1:1 line. It should be noted again that comparison results in Fig. 3 are only for those validation pixels (i.e., those 5% purposely removed non-missing pixels). The quantitative comparison results are given in Table I, and the mean, median, and standard deviation (STD) of the reconstructed/original ratio for the case of January 15, 2014 are 1.022, 0.996, and 0.261, respectively. Similar statistics results are obtained for the other three cases (Table I). The average values of mean, median, and STD from these four cases in Table I are 1.023, 0.991, and 0.295, respectively.

B. Ocean Features Revealed in the Reconstructed Global Daily Chl-a Data

The reconstructed daily images in Fig. 2 reveal many meso-scale and large-scale ocean features that are invisible in the original Chl-a images in Fig. 1. With the reconstructed (gap-filled) global Chl-a images, the oligotrophic waters (Chl-a concentration < 0.1 mg m^{-3}) in the center of the five subtropical ocean gyres, i.e., North Atlantic, South Atlantic, North Pacific, South Pacific, and South Indian Ocean, show the most obvious large-scale ocean features, which cover major parts of the global oceans. Equatorial Pacific Ocean and equatorial Atlantic Ocean regions have more enhanced Chl-a (~0.1–0.5 mg m^{-3}) than those in the subtropical gyres. In contrast, there is no significant increase of Chl-a in the equatorial Indian Ocean. On the other hand, high Chl-a concentrations are found in the high latitude regions in the North Atlantic Ocean, North Pacific Ocean, and Southern Ocean.

In addition to these large-scale features, the reconstructed

images also reveal many meso-scale ocean features, such as eddies and filaments associated with western boundary currents or coastal currents. The descriptions and locations of these meso-scale features are listed in Table II, and their locations are also marked in Fig. 2. Some of these features are warm-core eddies [57], such as the Loop Current (LC) eddies that have lower Chl-a concentrations, and some are cold-core eddies [57], such as eddies generated near Hawaii that have enhanced Chl-a concentrations.

All ocean features in Table II are dynamic since they vary with time. Figure 4 shows the transformation of a super North Brazil Current (NBC) ring [58] as an example. NBC rings are Earth's largest oceanic rings formed by the retroflection of the NBC near 8°N in the western tropical Atlantic [59]. The NBC is a western boundary current, which flows northward along Brazil's coast passing by the Amazon River mouth. The NBC separates from the South American coastline at 6°N–8°N and curves back on itself to feed the eastward North Equatorial Countercurrent (NECC) and close the clockwise wind-driven equatorial gyre [58]. The NBC occasionally curves back upon itself to pinch off large warm-core eddies. Figure 4 shows the formation and transformation of a super NBC ring with a diameter of ~500 km. On January 7, 2014, the NBC curved back but still did not completely closed itself (Fig. 4a), and the center of the ring was located at 9.18°N and 54.23°W (Fig. 4b). Six days later on January 13, 2014, the NBC formed a complete ring (Fig. 4c), and continued translating northwestward (Figs. 4d and 4e). By January 22, 2014, the center of the ring moved to 10.33°N and 56.95°W (Fig. 4f). Beginning on January 25, 2014, the ring started to transform from a circular shape to an elongated oval while moving further to the northwest (Figs. 4g–4i). It is also noted that a branch of the NBC flowed to the east and joined the NECC.

As another example, Fig. 5 shows the interaction of the LC with a spin-off eddy and the coastal waters in the West Florida Shelf (WFS). LC is a warm ocean current that flows northward between Cuba and the Yucatán Peninsula, moves north into the Gulf of Mexico, and loops east and south before exiting to the east through the Florida Straits [60]. Every 3 to 17 months, the "loop" spins off from the LC system and becomes a separate eddy [61]. Chl-a concentration within the LC and spin-off eddy
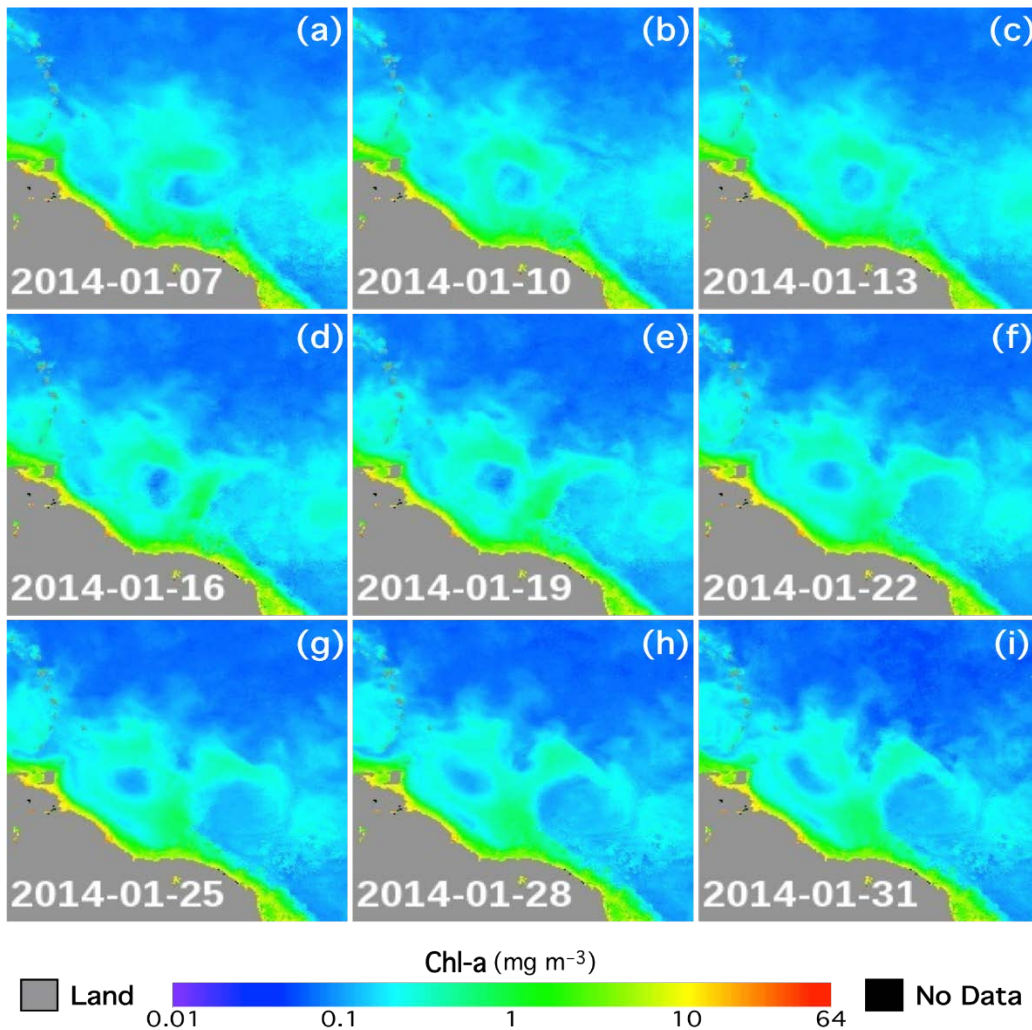
Fig. 4. The transformation progress for a super North Brazil Current ring in January 2014 using the reconstructed (gap-filled) VIIRS daily Chl-a images for panels (a)–(i) of January 7, 10, 13, 16, 19, 22, 25, 28, and 31, respectively.

is usually low due to their oligotrophic water source and the clockwise rotation as warm-core rings. Figure 5 shows a well-developed "loop" and an eddy to the north with very low Chl-a concentration (< 0.1 mg m^{-3}), and the WFS waters with high Chl-a concentration ($> {\sim}1$ mg m^{-3}). As seen in Fig. 5 from the VIIRS daily Chl-a spatial pattern progress, the LC extended northward from July 16 to July 31, 2014, as it moved closer to the eddy. As a result, the water with high Chl-a concentration between the eddy and loop current was squeezed out, and the WFS waters with high Chl-a concentration extended southward significantly from July 22 to July 31, 2014 (Figs. 5f–5i).

C. Gap Filling for Global 8-day and Monthly Chl-a Data

The global Level-3 8-day ocean color data are generated using the reconstructed (gap-filled) Level-3 daily data from the eight daily files. In the time-binning process for the Level-3 8-day data, the median is calculated as the 8-day value for each bin. Figure 6 shows examples of the reconstructed 8-day Chl-a images on January 9–16 (Fig. 6a), April 15–22 (Fig. 6b), July 12–19 (Fig. 6c), and October 8–15 (Fig. 6d) of 2014. The 8-day global Chl-a images are smoother spatially than those of daily

images (as expected), and the meso-scale features are still visible. The reconstructed 8-day Chl-a data are also compared with the original 8-day Chl-a data, which are generated by binning the original daily data. Figure 7 shows the density scatter plot of the reconstructed versus original 8-day Chl-a images (all common pixels are included), and the quantitative comparison results are listed in Table III. It is particularly noted that for the 8-day data comparison (Fig. 7) all common pixels from both original and new 8-day Chl-a data are used. Therefore, there are significantly more data in Fig. 7 than those in Fig. 3. The mean, median, and STD values for the ratio of the reconstructed/original for the case of January 9–16, 2014 are 0.984, 0.980, and 0.152, respectively. Similar statistics results are obtained for the other three 8-day cases (Table III). The average values of mean, median, and STD from these four 8-day cases in Table III are 0.983, 0.980, and 0.159, respectively.

Similarly, monthly global Level-3 ocean color data are reconstructed by binning the corresponding daily Level-3 data for the corresponding month. Figure 8 shows examples of the reconstructed monthly Chl-a images for January (Fig. 8a), April (Fig. 8b), July (Fig. 8c), and October (Fig. 8d) of 2014. The
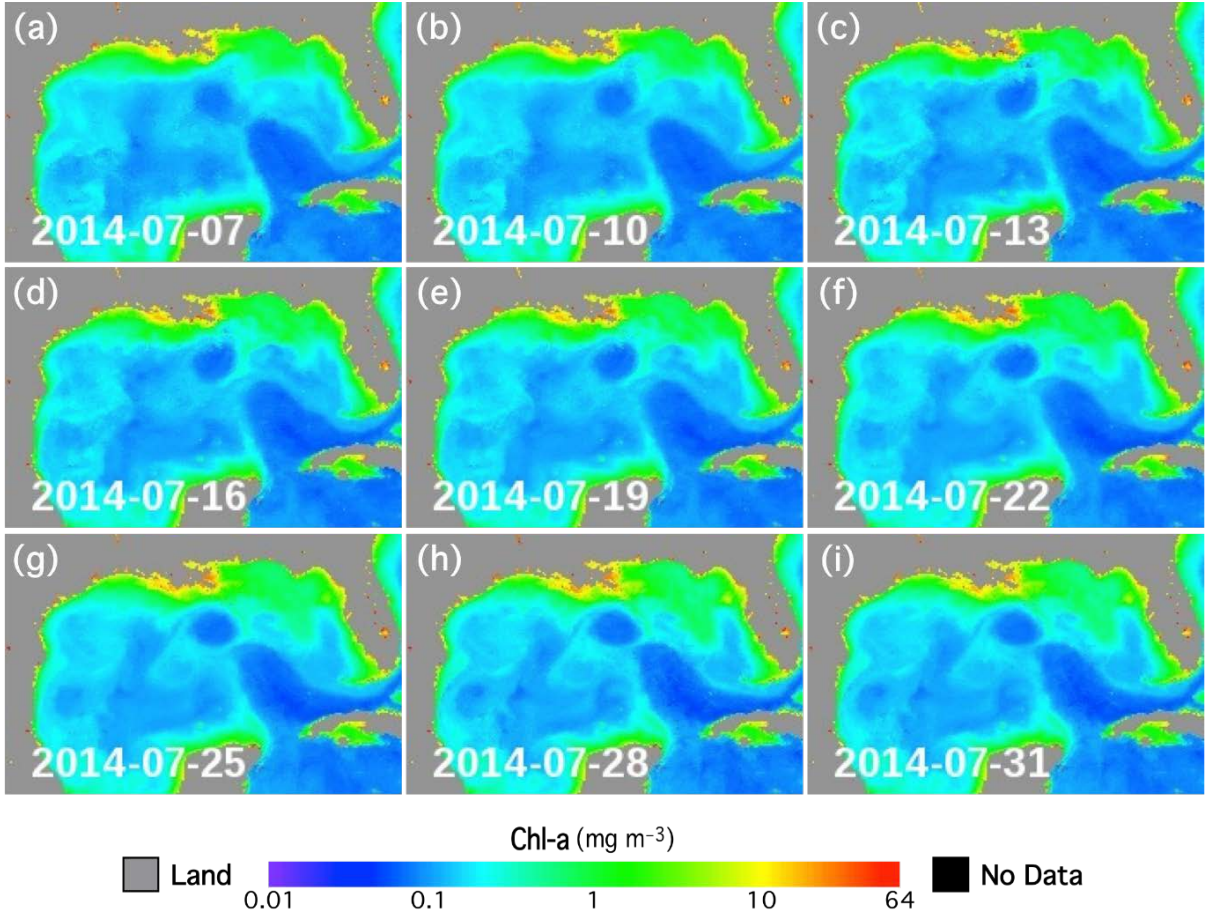
Fig. 5. Interaction of the LC, spin-off eddy, and coastal waters in the West Florida Shelf for the period of October 7–31, 2014 from the reconstructed images for panels (a)–(i) of July 7, 10, 13, 16, 19, 22, 25, 28, and 31, respectively.

monthly images are so smooth spatially that the meso-scale ocean features are actually averaged out. However, the seasonal variations are now observable in the reconstructed (non-gap) images. For example, the winter Chl-a bloom in the Arabian Sea and the spring bloom in the North Atlantic Ocean can now be seen in the reconstructed image of January (Fig. 8a) and April (Fig. 8b), respectively. The global reconstructed monthly Chl-a data are also compared with the original monthly data. Figure 9 shows the density scatter plot of the monthly-reconstructed Chl-a versus those from the original monthly data (all common pixels included), and the quantitative comparison results are listed in Table III. Again, in the monthly data comparisons in Fig. 9, all common pixels from both original and new monthly Chl-a data are used. The mean, median, and STD of the reconstructed/original ratio for the case of January of 2014 are 0.989, 0.988, and 0.125, respectively. Similar statistics results are obtained for the other three monthly cases (Table III). The average values of mean, median, and STD from these four monthly cases in Table III are 0.985, 0.987, and 0.126, respectively.

D. Gap Filling for Global $K_d(490)$ and $nL_w(\lambda)$ Data

To further test and evaluate the DINEOF efficacy for other

TABLE III. MEAN, MEDIAN, AND STD OF RECONSTRUCTED/ORIGINAL RATIO OF CHL-A FOR 8-DAY AND MONTHLY DATA.

Date Period in 2014	Mean	Median	STD
January 9-16	0.984	0.980	0.152
April 15-22	0.983	0.979	0.154
July 12-19	0.982	0.980	0.157
October 8-15	0.981	0.979	0.172
January (monthly)	0.989	0.988	0.125
April (monthly)	0.991	0.989	0.125
July (monthly)	0.981	0.987	0.116
October (monthly)	0.980	0.982	0.137

ocean color products, the same DINEOF procedure is applied to global daily $K_d(490)$ and $nL_w(\lambda)$ at the five VIIRS visible bands to reconstruct missing pixels, and the 8-day and monthly $K_d(490)$ and $nL_w(\lambda)$ are generated by binning the reconstructed (non-gap) daily data. Figure 10 shows examples of daily $K_d(490)$ images on January 15 (Fig. 10a) and April 15 (Fig. 10b), 8-day $K_d(490)$ images for July 12–19 (Fig. 10c) and a monthly $K_d(490)$ image for October (Fig. 10d) of 2014. Since $K_d(490)$ is highly correlated to Chl-a [62], especially in open
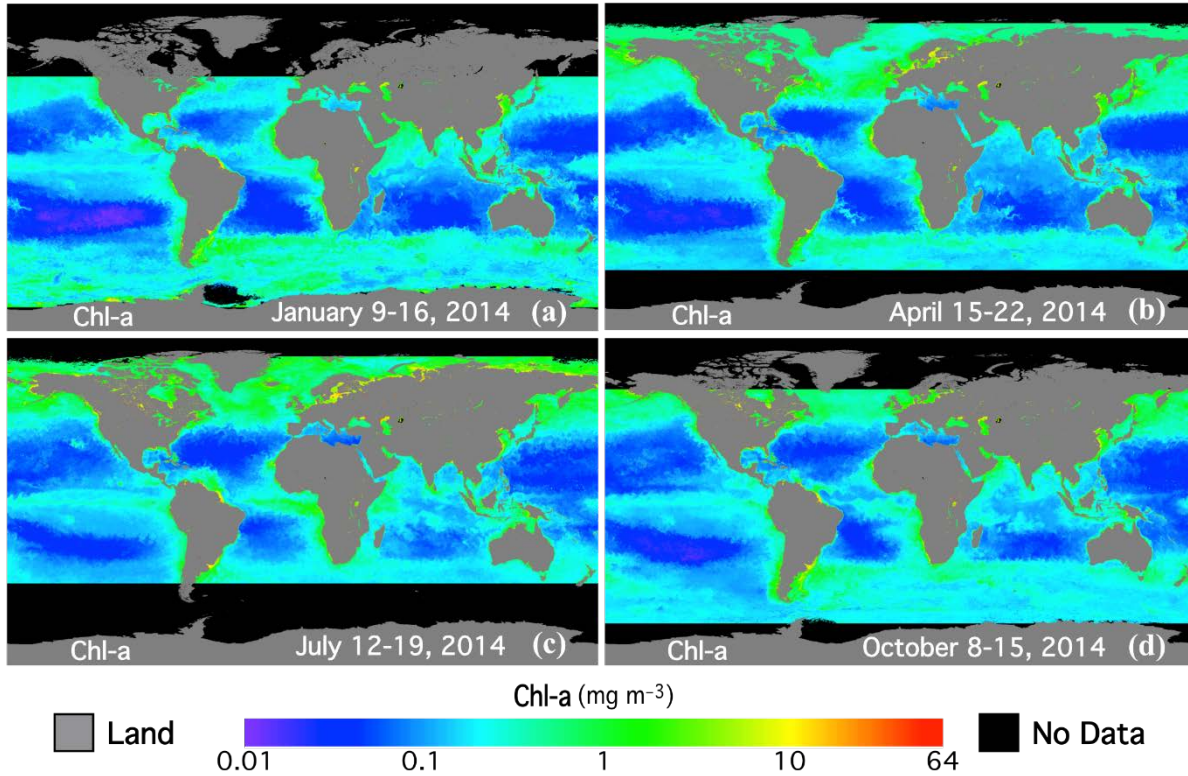
Fig. 6. Reconstructed (gap-filled) VIIRS global 8-day Chl-a images for the 8-day period of (a) January 9–16, (b) April 15–22, (c) July 12–19, and (d) October 8–15, 2014.
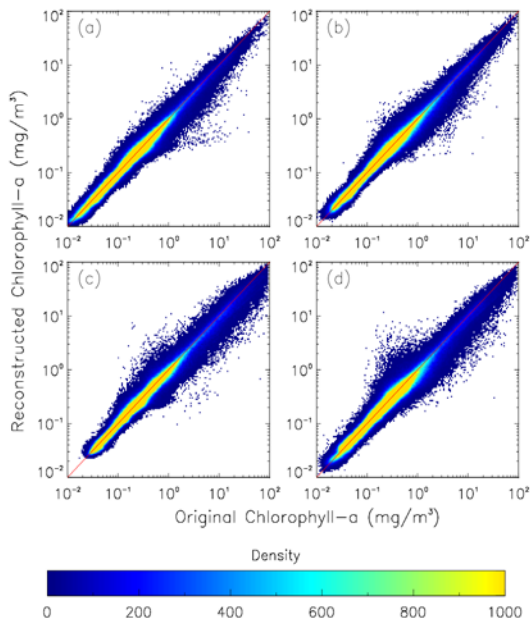

Fig. 7. Scatter plot of reconstructed versus original 8-day global Chl-a data for the 8-day period of (a) January 9–16, (b) April 15–22, (c) July 12–19, and (d) October 8–15, 2014.

Similarly, example images of the reconstructed daily, 8-day, and monthly $nL_w(443)$ and $nL_w(551)$ are shown in Fig. 11 and Fig. 12, respectively. As expected, while $nL_w(443)$ has the maximum values in the oligotrophic open oceans and minimum in the coastal/inland waters, $nL_w(551)$ is quite uniform spatially in the global open ocean. Global $nL_w(443)$ images in Fig. 11 also show seasonal variations, i.e., highs in the southern (northern) hemisphere ocean gyres in winter (summer), and lows in the northern (southern) hemisphere ocean gyres in summer (winter). On the other hand, the global $nL_w(551)$ images in Fig. 12 show a quite stable value throughout of the year, except over coastal and inland waters.

IV. DISCUSSIONS AND SUMMARY

In VIIRS-derived ocean color product data, there are many missing pixels (spatial gaps) due to cloud cover, high sun glint contamination, large solar- and sensor-zenith angles, and various other reasons. In this study, the DINEOF method is used to reconstruct and gap-fill missing data in VIIRS global Level-3 daily binned data files for seven ocean color products, i.e., Chl-a, $K_d(490)$, $nL_w(410)$, $nL_w(443)$, $nL_w(486)$, $nL_w(551)$, and $nL_w(671)$. Since the number of bins is quite large in global Level-3 data with 9-km spatial resolution, the global dataset is divided into 16 zonal sections, and DINEOF is applied on each of the sections simultaneously to improve data processing efficiency. The VIIRS global 8-day and monthly Level-3 ocean color data are then generated using the daily-reconstructed (non-gap) data. In the reconstructed daily Chl-a images, the
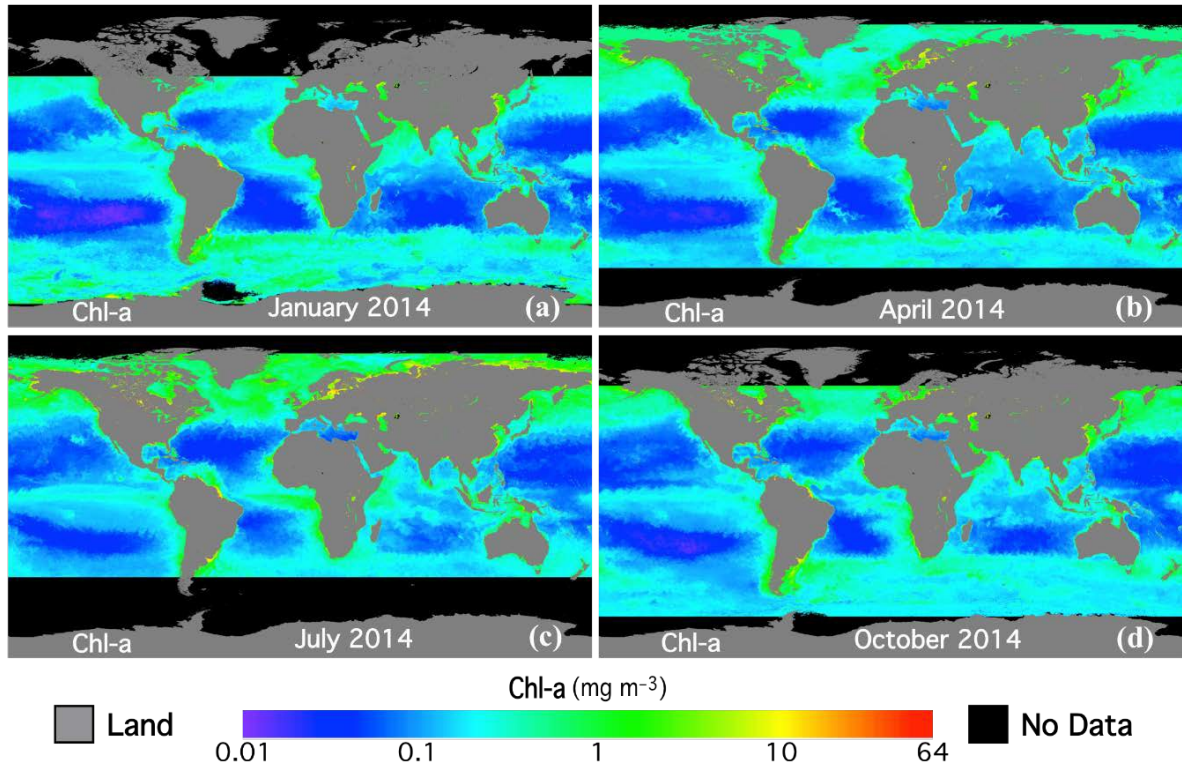
oceans, the meso-scale and large-scale ocean features in the reconstructed (non-gap) $K_d(490)$ images are generally similar to those in the Chl-a daily, 8-day, and monthly images.

Fig. 8. Reconstructed (gap-filled) VIIRS monthly Chl-a images for the month in 2014 of (a) January, (b) April, (c) July, and (d) October.
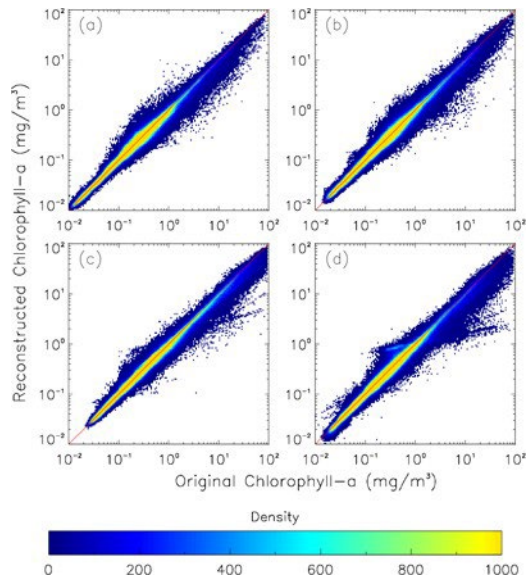
no data discontinuities between gap-filled and non-gap data. In addition, the temporal variation of these meso-scale and large-scale ocean dynamic features are also smooth from the reconstructed (non-gap) images. To quantitatively evaluate the accuracy of the DINEOF data reconstruction method, a set of valid pixels are intentionally treated as "missing pixels," so that DINEOF-reconstructed data can be compared with the original ("truth") data. Quantitative comparison results show that the approach is valid and reasonable for gap-filling missing data in VIIRS global Level-3 ocean color product data. In fact, average values of the mean, median, and STD of the VIIRS daily Chl-a reconstructed/original ratio are 1.023, 0.991, and 0.295, respectively.

The reconstructed 8-day and monthly VIIRS global Level-3 Chl-a data are also evaluated. The reconstructed 8-day and monthly images are smoother spatially than those from daily images. The meso-scale features are still visible in the 8-day images, but they are averaged out in the monthly images. The seasonal variations of some ocean features, such as the winter bloom in the Arabia Sea and the spring bloom in the North Atlantic Ocean, are also reconstructed and well captured. In addition, the reconstructed 8-day and monthly Chl-a data are compared with original data for validation. Results show that the reconstructed 8-day and monthly data are reasonably accurate. Furthermore, the DINEOF method is also applied to $K_d(490)$ and $nL_w(\lambda)$ at the VIIRS five visible bands to reconstruct missing data. The spatial and temporal variations in $K_d(490)$ are similar to Chl-a. As expected, $nL_w(443)$ is at its maximum in the oligotrophic open oceans and at its minimum

Fig. 9. Scatter plots of reconstructed versus original monthly Chl-a for the month in 2014 of (a) January, (b) April, (c) July, and (d) October.

transition between the gap and non-gap pixels is quite smooth spatially (no discontinuity boundaries), and both the meso-scale and large-scale ocean features are well captured in the reconstructed (non-gap) images. This is an important advantage in using the reconstructed DINEOF approach, which will have
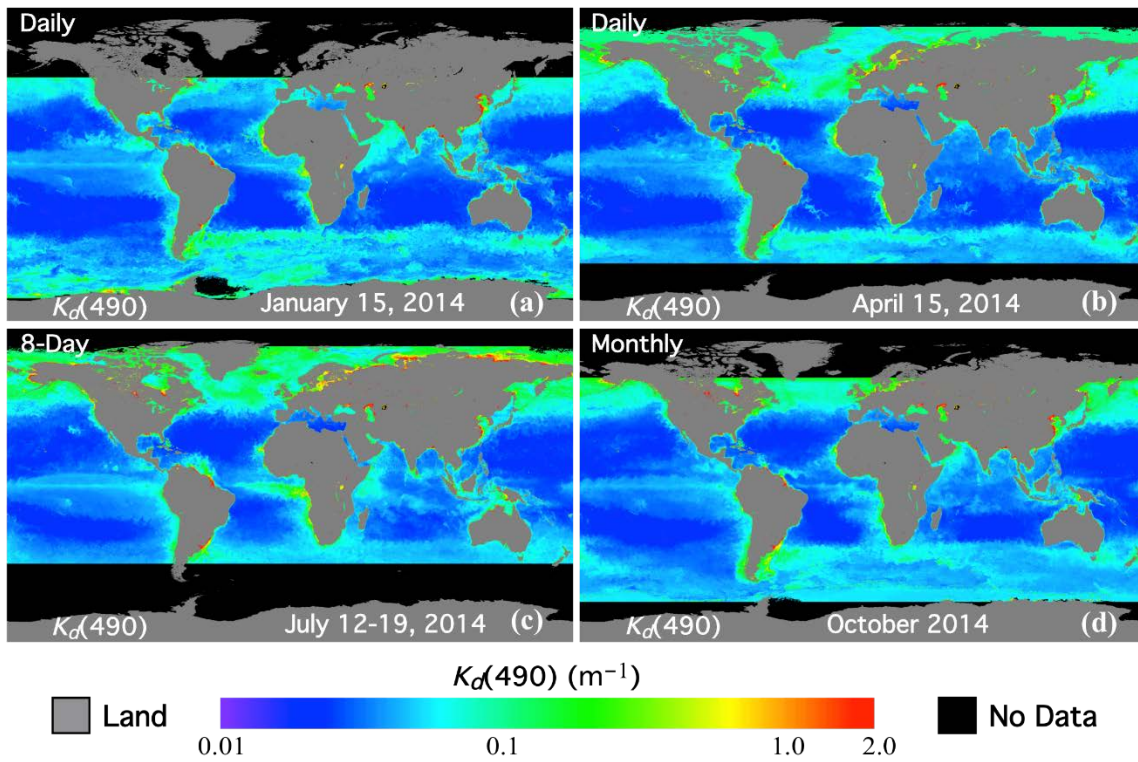
Fig. 10. Reconstructed (gap-filled) daily, 8-day, and monthly $K_d(490)$ images for the month in 2014 of (a) January, (b) April, (c) July, and (d) October.
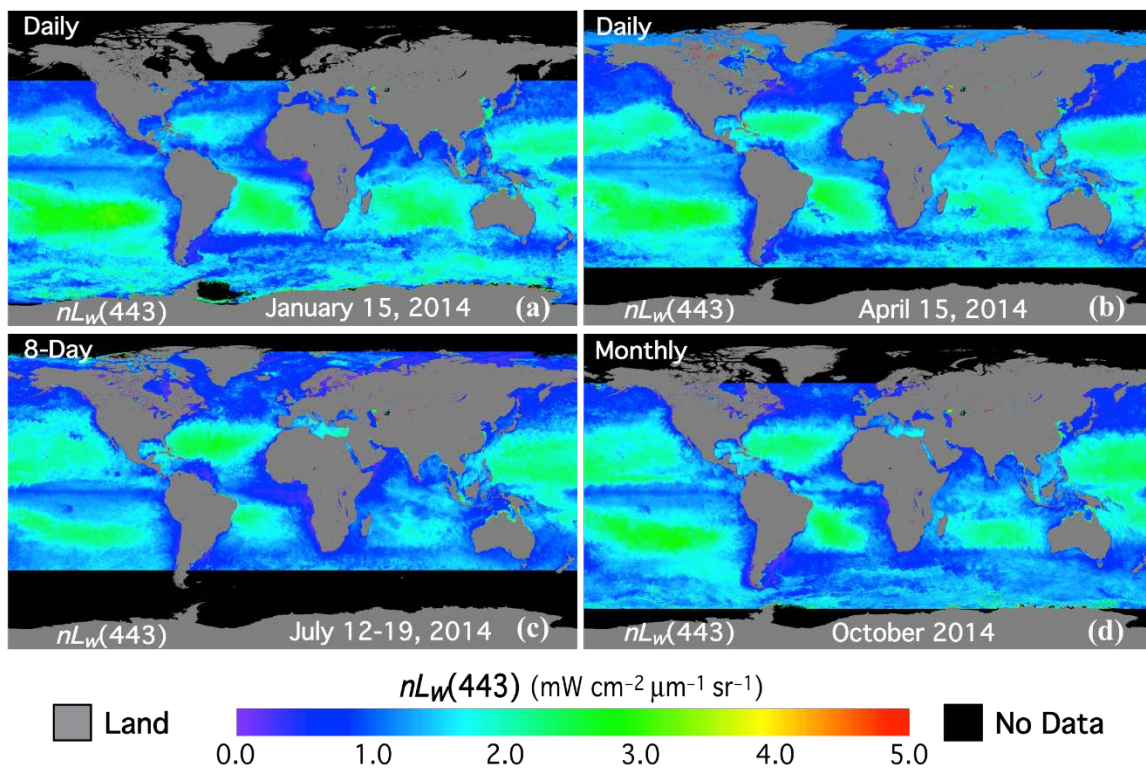

Fig. 11. Reconstructed (gap-filled) daily, 8-day, and monthly $nL_w(443)$ images for the month in 2014 of (a) January, (b) April, (c) July, and (d) October.

in the coastal waters, and also show strong seasonal variations. On the other hand, $nL_w(551)$ is quite uniform over global open oceans both spatially and temporally, except over coastal and inland waters.
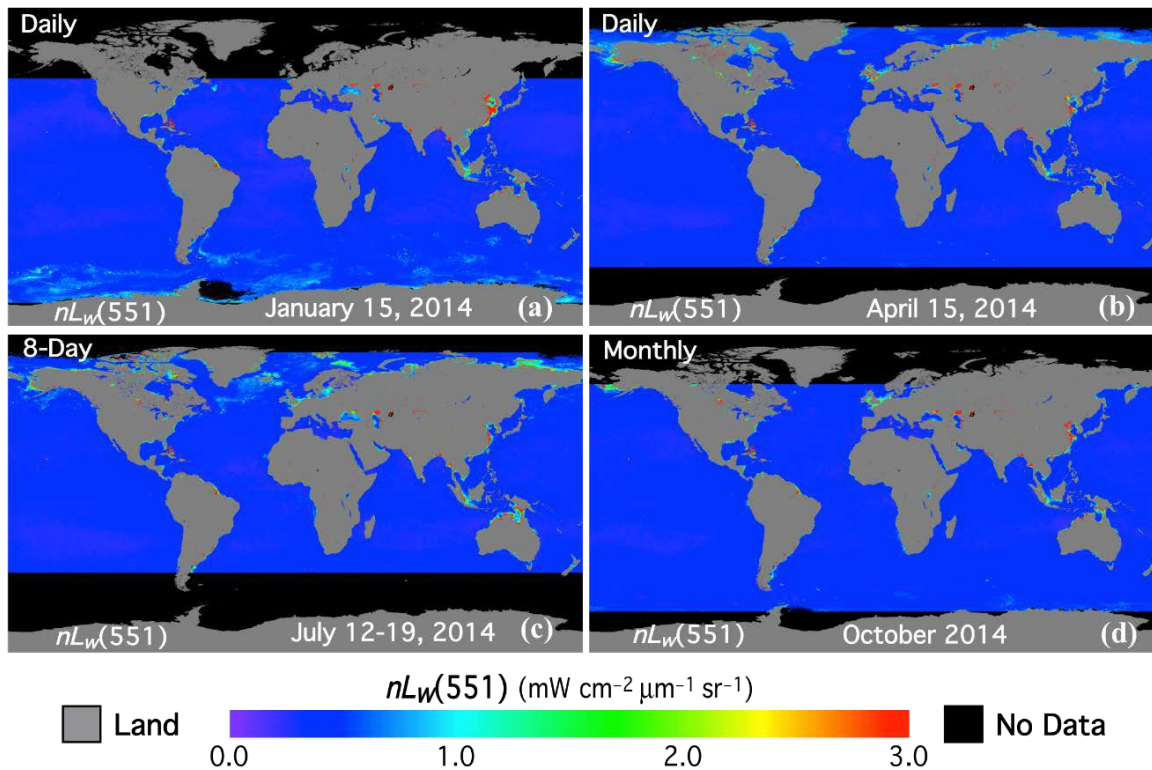
Fig. 12. Reconstructed (gap-filled) daily, 8-day, and monthly $nL_w(551)$ images for the month in 2014 of (a) January, (b) April, (c) July, and (d) October.

Results in this study show that the DINEOF method can successfully reconstruct meso-scale and large-scale spatial features in the global VIIRS Level-3 daily images, as well as the temporal variation of these ocean features. However, due to high solar-zenith angle, there are no pixels available for the entire month in the large areas of the northern high latitude region in January and the southern high latitude region in July. For those missing pixels, DINEOF can only replace them with a global mean value without spatial and temporal variations. Therefore, those missing pixels in high latitude regions cannot be reconstructed using the DINEOF method.

Finally, results in this study show that, using the DINEOF method with the proposed data processing approach, VIIRS daily ocean color products can be routinely produced without gaps, providing useful global ocean color product data for research and various applications in the ocean community.

The views, opinions, and findings contained in this paper are those of the authors and should not be construed as an official NOAA or U.S. Government position, policy, or decision.

REFERENCES

[1]   C. R. McClain, G. C. Feldman, and S. B. Hooker, "An overview of the SeaWiFS project and strategies for producing a climate research quality global ocean bio-optical time series," *Deep Sea Res. Part II*, vol. 51, pp. 5–42, 2004.
[2]   W. E. Esaias, M. R. Abbott, I. Barton, O. B. Brown, J. W. Campbell, K. L. Carder, D. K. Clark, R. L. Evans, F. E. Hodge, H. R. Gordon, W. P. Balch, R. Letelier, and P. J. Minnet, "An overview of MODIS capabilities for ocean science observations," *IEEE Trans. Geosci. Remote Sens.*, vol. 36, pp. 1250–1265, 1998.
[3]   V. V. Salomonson, W. L. Barnes, P. W. Maymon, H. E. Montgomery, and H. Ostrow, "MODIS: advanced facility instrument for studies of the Earth as a system," *IEEE Trans. Geosci. Remote Sens.*, vol. 27, pp. 145–153, 1989.
[4]   M. Rast, J. L. Bezy, and S. Bruzzi, "The ESA Medium Resolution Imaging Spectrometer MERIS a review of the instrument and its mission," *Int. J. Remote Sens.*, vol. 20, pp. 1681–1702, 1999.
[5]   M. D. Goldberg, H. Kilcoyne, H. Cikanek, and A. Mehta, "Joint Polar Satellite System: The United States next generation civilian polar-orbiting environmental satellite system," *J. Geophys. Res. Atmos.*, vol. 118, pp. 13463–13475, doi: 10.1002/2013JD020389, 2013.
[6]   M. Wang, X. Liu, L. Tan, L. Jiang, S. Son, W. Shi, K. Rausch, and K. Voss, "Impact of VIIRS SDR performance on ocean color products," *J. Geophys. Res. Atmos.*, vol. 118, pp. 10347–10360, doi:10.1002/jgrd.50793, 2013.
[7]   A. B. Kara, A. J. Wallcraft, and H. E. Hurlburt, "A new solar radiation penetration scheme for use in ocean mixed layer studies: An applications to the Black Sea using a fine-resolution Hybrid Coordinate Ocean Model (HYCOM)," *J. Phys. Oceanogr.*, vol. 35, 2005.

[8] M. Wang, L. Jiang, X. Liu, S. Son, J. Sun, W. Shi, L. Tan, K. Mikelsons, X. Wang, and V. Lance, "VIIRS ocean color products: A progress update," *Proc. the IEEE Int. Geosci. Remote Sens. Symposium (IGARSS)*, pp. 5848–5851, Beijing, China, July 10-15, http://dx.doi.org/10.1109/IGARSS.2016.7730528, 2016.

[9] H. R. Gordon and M. Wang, "Retrieval of water-leaving radiance and aerosol optical thickness over the oceans with SeaWiFS: A preliminary algorithm," *Appl. Opt.*, vol. 33, pp. 443–452, 1994.

[10] IOCCG, "Atmospheric Correction for Remotely-Sensed Ocean-Colour Products," in *Reports of the International Ocean-Colour Coordinating Group*, vol. No. 10, M. Wang, Ed. IOCCG, Dartmouth, Canada, 2010.

[11] J. E. O'Reilly, S. Maritorena, B. G. Mitchell, D. A. Siegel, K. L. Carder, S. A. Garver, M. Kahru, and C. R. McClain, "Ocean color chlorophyll algorithms for SeaWiFS," *J. Geophys. Res.*, vol. 103, pp. 24937–24953, 1998.

[12] C. Hu, Z. Lee, and B. A. Franz, "Chlorophyll a algorithms for oligotrophic oceans: A novel approach based on three-band reflectance difference," *J. Geophys. Res.*, vol. 117, pp. C01011, doi: 10.1029/2011JC007395, 2012.

[13] M. Wang and S. Son, "VIIRS-derived chlorophyll-a using the ocean color index method," *Remote Sens. Environ.*, vol. 182, pp. 141–149, 2016.

[14] M. Wang, S. Son, and J. L. W. Harding, "Retrieval of diffuse attenuation coefficient in the Chesapeake Bay and turbid ocean regions for satellite ocean color applications," *J. Geophys. Res.*, vol. 114, C10011, doi:10.1029/2009JC005286, 2009.

[15] S. Son and M. Wang, "Diffuse attenuation coefficient of the photosynthetically available radiation Kd(PAR) for global open ocean and coastal waters," *Remote Sens. Environ.*, vol. 159, pp. 250–258, 2015.

[16] Z. P. Lee, K. L. Carder, and R. A. Arnone, "Deriving inherent optical properties from water color: a multiple quasi-analytical algorithm for optically deep waters," *Appl. Opt.*, vol. 41, pp. 5755–5772, 2002.

[17] J. Wei, Z. Lee, and S. Shang, "A system to measure the data quality of spectral remote-sensing reflectance of aquatic environments," *J. Geophys. Res. Oceans*, vol. 121, pp. 8189–8207, 2016.

[18] M. Wang, "Remote sensing of the ocean contributions from ultraviolet to near-infrared using the shortwave infrared bands: simulations," *Appl. Opt.*, vol. 46, pp. 1535–1547, 2007.

[19] M. Wang and W. Shi, "The NIR-SWIR combined atmospheric correction approach for MODIS ocean color data processing," *Opt. Express*, vol. 15, pp. 15722–15733, doi:10.1364/oe.15.015722, 2007.

[20] M. Wang and W. Shi, "Estimation of ocean contribution at the MODIS near-infrared wavelengths along the east coast of the U.S.: Two case studies," *Geophys. Res. Lett.*, vol. 32, L13606, doi:10.1029/2005GL022917, 2005.

[21] M. Wang, W. Shi, and J. Tang, "Water property monitoring and assessment for China's inland Lake Taihu from MODIS-Aqua measurements," *Remote Sens. Environ.*, vol. 115, pp. 841–854, 2011.

[22] M. Wang, S. Son, and W. Shi, "Evaluation of MODIS SWIR and NIR-SWIR atmospheric correction algorithm using SeaBASS data," *Remote Sens. Environ.*, vol. 113, pp. 635–644, 2009.

[23] J. Sun and M. Wang, "Radiometric calibration of the VIIRS reflective solar bands with robust characterizations and hybrid calibration coefficients," *Appl. Opt.*, vol. 54, pp. 9331–9342, 2015.

[24] S. A. Ackerman, K. I. Strabala, W. P. Menzel, R. A. Frey, C. C. Moeller, and L. E. Gumley, "Discriminating clear sky from clouds with MODIS," *J. Geophys. Res.*, vol. 103, pp. 32141–32157, 1998.

[25] M. Wang and W. Shi, "Cloud masking for ocean color data processing in the coastal regions," *IEEE Trans. Geosci. Remote Sens.*, vol. 44, pp. 3196–3205, doi:10.1109/tgrs.2006.876293, 2006.

[26] M. Wang and S. Bailey, "Correction of the sun glint contamination on the SeaWiFS ocean and atmosphere products," *Appl. Opt.*, vol. 40, pp. 4790–4798, 2001.

[27] R. W. Preisendorfer and C. D. Mobley, *Principal component analysis in meteorology and oceanography*. Amsterdam: Elsevier, 1988.

[28] H. Shen, X. Li, Q. Cheng, C. Zeng, G. Yang, H. Li, and L. Zhang, "Missing information reconstruction of remote sensing data: a technical review," *IEEE Geosci. Remote Sens. Magazine*, vol. 3, pp. 61–85, 2015.

[29] J. Beckers and M. Rixen, "EOF calculations and data filling from incomplete oceanographic data sets," *J. Atmos. Ocean Technol.*, vol. 20, pp. 1839–1856, 2003.

[30] A. Alvera-Azcarate, A. Barth, M. Rixen, and J. Beckers, "Reconstruction of incomplete oceanographic data sets using Empirical Orthogonal Functions. Application to the Adriatic Sea," *Ocean Modeling*, vol. 9, pp. 325–346, 2005.

[31] U. Ganzedo, A. Alvera-Azcarate, G. Esnaola, A. Ezcurra, and J. Saenz, "Reconstruction of sea surface temperature by means of DINEOF. A case

study during the fishing season in the Bay of Biscay," *Int. J. Remote Sens.*, vol. 32, pp. 933–950, 2011.

[32] E. Mauri, P. M. Poulain, and Z. Juznic-Zontac, "MODIS chlorophyll variability in the northern Adriatic Sea and relationship with forcing parameters," *J. Geophys. Res.*, vol. 112, C03S11, doi:10.1029/2006JC003545, 2007.

[33] E. Mauri, P. M. Poulain, and G. Notarstefano, "Spatial and temporal variability of the sea surface temperature in the Gulf of Trieste between January 2000 and December 2006," *J. Geophys. Res.*, vol. 113, C10012, doi: 10.1029/2007JC004537, 2008.

[34] B. Nechad, A. Alvera-Azcarate, K. Ruddick, and N. Greenwood, "Reconstruction of MODIS total suspended matter time series maps by DINEOF and validation with autonomous platform data," *Ocean Dynamics*, vol. 61, pp. 19205–1214, 2011.

[35] D. Sirjacobs, A. Alvera-Azcarate, A. Barth, G. Lacroix, Y. Park, B. Nechad, K. Ruddick, and J. Beckers, "Cloud filling of ocean color and sea surface temperature remote sensing products over the Southern North Sea by the data interpolating empirical orthogonal functions methodology," *J. Sea Res.*, vol. 65, pp. 114–130, 2011.

[36] G. Volpe, B. B. Nardelli, P. Cipollini, R. Santoleri, and I. S. Robinson, "Seasonal to interannual phytoplankton response to physical processes in the Mediterranean Sea from satellite observations," *Remote Sens. Environ.*, vol. 117, pp. 223–235, 2012.

[37] Y. Li and R. He, "Spatial and temporal variability of SST and ocean color in the Gulf of Maine based on cloud-free SST and chlorophyll reconstructions in 2003–2012," *Remote Sens. Environ.*, vol. 144, pp. 98–108, 2014.

[38] M. Moradi and K. Kabiri, "Spatio-temporal variability of SST and chlorophyll-a from MODIS data in the Persian Gulf," *Marine Pollution Bulletin*, vol. 98, pp. 14–25, 2015.

[39] T. Shropshire, Y. Li, and R. He, "Storm impact on sea surface temperature and chlorophyll a in the Gulf of Mexico and Sargasso Sea based on daily cloud-free satellite data reconstructions," *Geophy. Res. Lett.*, vol. 43, pp. 12199–12207, doi: 10.1002/2016GL071178, 2016.

[40] A. Alvera-Azcarate, Q. Vanhellemont, K. G. Ruddick, A. Barth, and J.-M. Beckers, "Analysis of high frequency geostationary ocean colour data using DINEOF," *Estuarine, Coastal and Shelf Science*, vol. 159, pp. 28–36, 2015.

[41] X. Liu and M. Wang, "Analysis of diurnal variations from the Korean Geostationary Ocean Color Imager measurements using the DINEOF method," *Estuar. Coast. Shelf Sci.*, pp. 230–241, 2016.

[42] B. Henn, M. S. Raleigh, A. Fisher, and J. D. Lundquist, "A comparison of methods for filling gaps in hourly near-surface air temperature data," *J. Hydrometeorology*, vol. 14, pp. 929–945, 2013.

[43] M. Wang, "A sensitivity study of SeaWiFS atmospheric correction algorithm: Effects of spectral band variations," *Remote Sens. Environ.*, vol. 67, pp. 348–359, 1999.

[44] M. Wang and B. A. Franz, "Comparing the ocean color measurements between MOS and SeaWiFS: A vicarious intercalibration approach for MOS," *IEEE Trans. Geosci. Remote Sens.*, vol. 38, pp. 184–197, 2000.

[45] M. Wang, A. Isaacman, B. A. Franz, and C. R. McClain, "Ocean color optical property data derived from the Japanese Ocean Color and Temperature Scanner and the French Polarization and Directionality of the Earth's Reflectances: A comparison study," *Appl. Opt.*, vol. 41, pp. 974–990, 2002.

[46] W. Shi and M. Wang, "Satellite views of the Bohai Sea, Yellow Sea, and East China Sea," *Prog. Oceanogr.*, vol. 104, pp. 35–45, 2012.

[47] W. Shi, M. Wang, and L. Jiang, "Spring-neap tidal effects on satellite ocean color observations in the Bohai Sea, Yellow Sea, and East China Sea," *J. Geophys. Res.*, vol. 116, C12032, doi:10.1029/2010JC007234, 2011.

[48] W. Shi and M. Wang, "Ocean reflectance spectra at the red, near-infrared, and shortwave infrared from highly turbid waters: A study in the Bohai Sea, Yellow Sea, and East China Sea," *Limnol. Oceanogr.*, vol. 59, pp. 427–444, 2014.

[49] S. Son and M. Wang, "Water properties in Chesapeake Bay from MODIS-Aqua measurements," *Remote Sens. Environ.*, vol. 123, pp. 163–174, 2012.

[50] M. Wang, C. J. Nim, S. Son, and W. Shi, "Characterization of turbidity in Florida's Lake Okeechobee and Caloosahatchee and St. Lucie estuaries using MODIS-Aqua measurements," *Water Research*, vol. 46, pp. 5410–5422, 2012.

[51] W. Shi and M. Wang, "Satellite observations of flood-driven Mississippi River plume in the spring of 2008," *Geophy. Res. Lett.*, vol. 36, L07607, doi:10.1029/2009GL037210, 2009.

[52] M. Wang and X. Liu, "MODIS Ocean Color Products Using the SWIR Method," pp. MODIS-SWIR Algorithm Theoretical Basis Document (ATBD), 40 pp., NOAA Product System Development and Implementation (PSDI), 2012.

[53] M. Wang, J. H. Ahn, L. Jiang, W. Shi, S. Son, Y. J. Park, and J. H. Ryu, "Ocean color products from the Korean Geostationary Ocean Color Imager (GOCI)," *Opt. Express*, vol. 21, pp. 3835–3849, 2013.

[54] J. W. Campbell, J. M. Blaisdell, and M. Darzi, "Level-3 SeaWiFS Data Products: Spatial and Temporal Binning Algorithms," NASA Goddard Space Flight Center, Greenbelt, Maryland Vol. 32, NASA Tech. Memo. 104566, S.B. Hooker, E.R. Firestone, and J.G. Acker, Eds., 1995.

[55] L. Jiang and M. Wang, "Identification of pixels with stray light and cloud shadow contaminations in the satellite ocean color data processing," *Appl. Opt.*, vol. 52, pp. 6757–6770, 2013.

[56] M. Wang and W. Shi, "Detection of ice and mixed ice-water pixels for MODIS ocean color data processing," *IEEE Trans. Geosci. Remote Sens.*, vol. 47, pp. 2510–2518, 2009.

[57] J. H. Steele, S. A. Thorpe, and K. K. Turekian, *Ocean Currents: A derivative of the encyclopedia of Ocean Sciences*: Academic Press, 2010.

[58] W. E. Johns, T. N. Lee, F. A. Schott, R. J. Zantopp, and R. H. Evans, "The North Brazil Current retroflection: Seasonal structure and eddy variability," *J. Geophys. Res.*, vol. 95, pp. 22103–22120, 1990.

[59] D. M. Fratantoni and D. A. Glickson, "North Brazil Current ring generation and evolution observed with SeaWiFS," *J. Phys. Oceanogr.*, vol. 32, pp. 1058–1074, 2002.

[60] P. S. Fratantoni, N. T. Lee, G. P. Podesta, and F. Muller-Karger, "The influence of Loop Current perturbations on the formation and evolution of Tortugas eddies in the southern Straits of Florida," *J. Geophys. Res. Oceans*, vol. 103, pp. 24759–24779, 1998.

[61] W. Sturges and R. Leben, "Frequency of ring separations from the Loop Current in the Gulf of Mexico: A revised estimate," *J. Phys. Oceanogr.*, vol. 30, pp. 1814–1819, 2000.

[62] A. Morel, Y. Huot, B. Gentili, P. J. Werdell, S. B. Hooker, and B. A. Franz, "Examining the consistency of products derived from various ocean color sensors in open ocean (Case 1) waters in the perspective of a multi-sensor approach," *Remote Sens. Environ.*, vol. 111, pp. 69–88, 2007.

Xiaoming Liu received the B.S. degree in physical oceanography from the Ocean University of Qingdao, Qingdao, China, in 1991, and the M.S. (in 1998) and Ph.D. degree (in 2006), both in marine science from North Carolina State University, Raleigh, NC.

Since May of 2006, he has been with the Center for Satellite Applications and Research (STAR), National Oceanic and Atmospheric Administration (NOAA) National Environmental Satellite, Data, and Information Service (NESDIS), College Park, Maryland. He has been working at the STAR Ocean Color Research Team since August 2012. His research interests are in ocean color algorithm development, calibration and validation, physical/biological ocean numerical modeling, ocean color data processing software/system development, as well as various applications in both coastal areas and ocean basins using the ocean color remote sensing data.
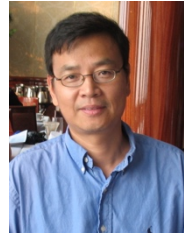
Menghua Wang received the B.S. degree in physics from the Zhejiang University, Hangzhou, China, in 1982, the M.S. degree in physics (with distinction) from California State University, Northridge, in 1987, and the Ph.D. degree in physics from the University of Miami, Coral Gables, Florida, in 1991.

Since January of 2005, he has been with the Center for Satellite Applications and Research (STAR), National Oceanic and Atmospheric Administration (NOAA) National Environmental Satellite, Data, and Information Service (NESDIS), College Park, Maryland. He has been the Chief of the Marine Ecosystems and Climate Branch at NOAA STAR since 2010. His research experiences include radiative transfer modeling, ocean color remote sensing, remote retrievals and in situ measurements of aerosol and cloud optical and microphysical properties, development of calibration and validation techniques, and development of strategy and techniques for the data processing and data merging from the multiple ocean color sensors, development of the end-to-end satellite ocean color data processing system, as well as various applications in open ocean and coastal/inland water regions using satellite and in situ measurements.